Supporting Information

High Performance Polarization-sensitive Self-Powered Imaging photodetectors based on p-Te/n-$MoSe_2$ van der Waals Heterojunction with strong interlayer transition

Qixiao Zhao,[ab] Feng Gao,[c] Hongyu Chen,*[ab] Wei Gao,[ab] Mengjia Xia,[ab] Yuan Pan,[ab] Hongyan Shi,[d] Shichen Su,[abe] Xiaosheng Fang,*[f] and Jingbo Li*[ab]

a. Institute of Semiconductor Science and Technology, South China Normal University, Guangzhou 510631, P.R. China.
b. Guangdong Province Key Lab of Chip and Integration Technology, Guangzhou 510631, P.R. China.
c. Key Laboratory of Micro-systems and Micro-structures Manufacturing of Ministry of Education, Harbin Institute of Technology, Harbin 150080, P.R. China.
d. Department of Physics, Harbin Institude of Technology, Harbin 150080, P. R. China.
e. SCNU Qingyuan Institute of Science and Technology Innovation Co., Ltd, Qingyuan 511517, P. R. China.
f. Department of Materials Science, Fudan University, Shanghai 200433, P. R. China.

Email: chenhy@m.scnu.edu.cn; xshfang@fudan.edu.cn; jbli@m.scnu.edu.cn

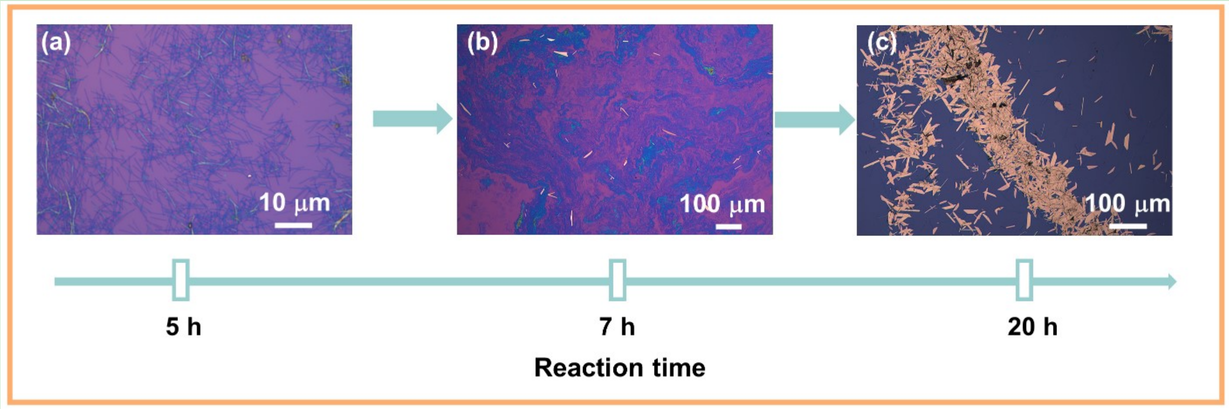

Fig. S1 Growth mechanism of solution-grown Te nanosheets. (a-c) Optical image of morphology evolution from the nanowire (a) through intermediate state (b) to the nanosheets (c) of Te grown by solution-grown.

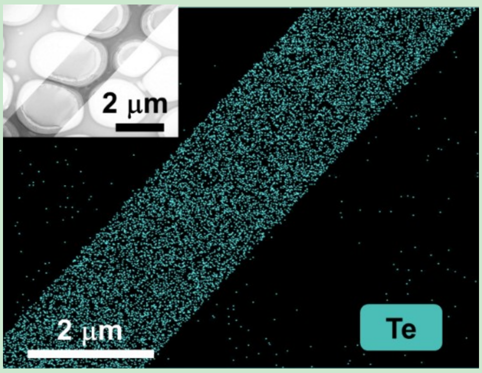

Fig. S2 EDS elemental mapping for Te nanosheet. Inset: low- magnification TEM image of Te nanosheet.

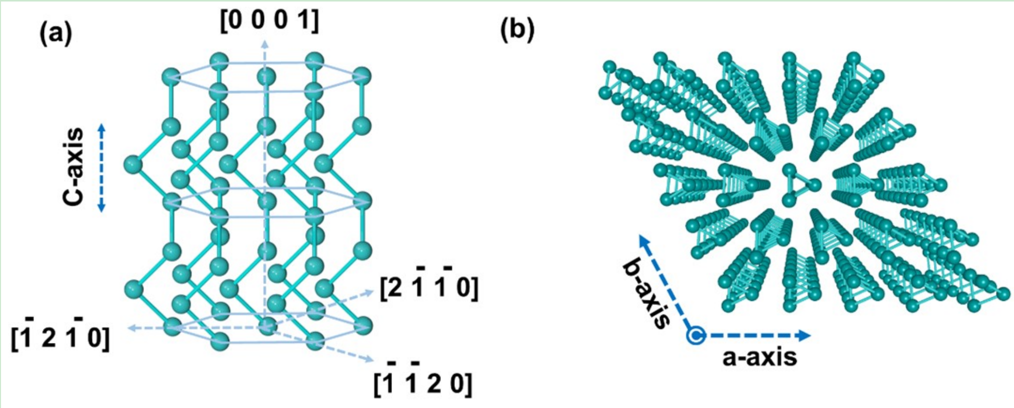

Fig. S3 Nanostructure for 2D Te nanosheet. (a-b) Crystal structure of Te nanosheet viewed from the b-axis (a) and viewed from the c-axis (b).

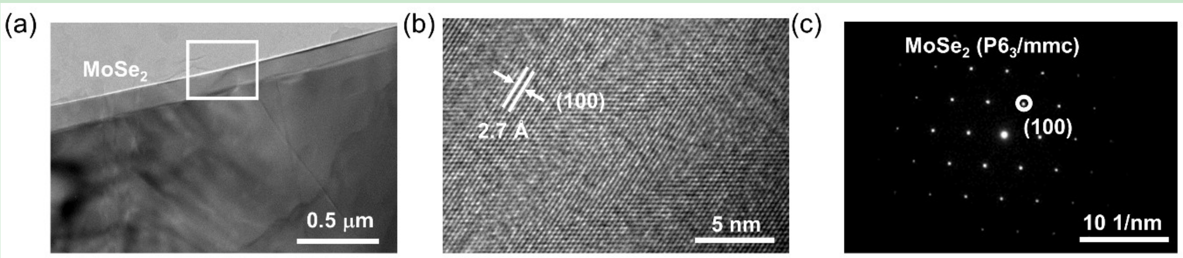

Fig. S4 Material characterization of $MoSe_2$ nanosheet. (a) Low-magnification TEM image of $MoSe_2$ nanosheet. (b) HR-TEM image taken from the $MoSe_2$ nanosheet. (c) Diffraction pattern of $MoSe_2$ nanosheet.

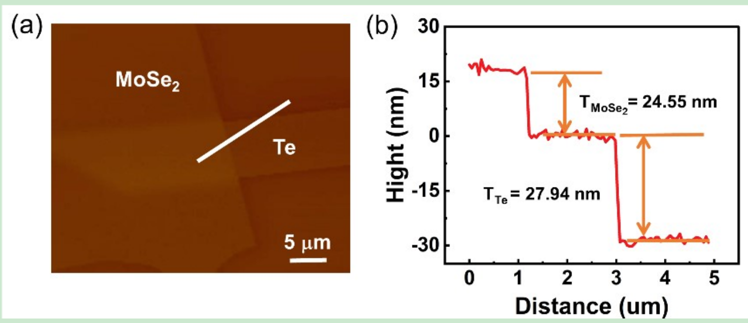

Fig. S5 AFM image of p-Te/n-$MoSe_2$ heterojunction device.

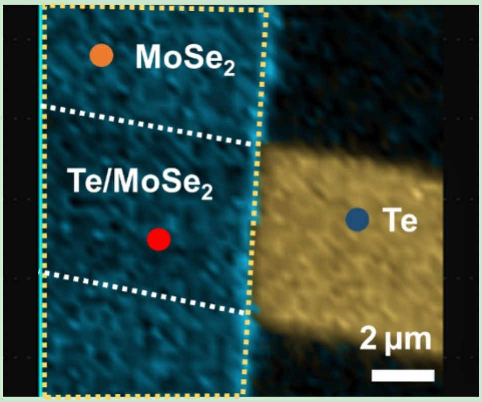

Fig. S6 Raman intensity mapping collected at A_1 (Te: 119 cm^{-1}) and A_{1g} ($MoSe_2$: 238 cm^{-1}).

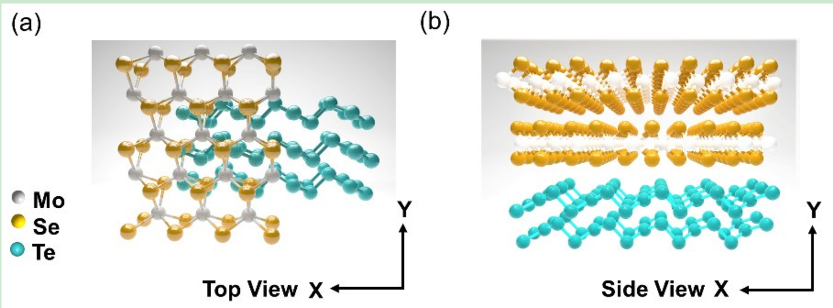

Fig. S7 Top view (a) and side view (b) crystal structure of p-Te/n-$MoSe_2$ heterojunction.

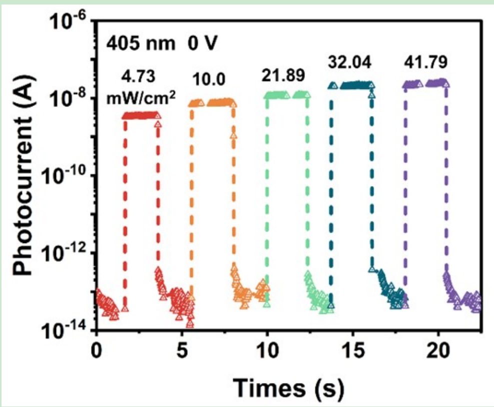

Fig. S8 Time-resolved photovoltaic response of the heterostructure under different laser powers intensity of 405 nm at V = 0 V.

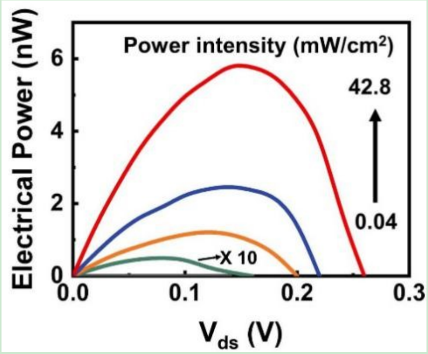

Fig. S9 Electrical power under varied power intensities (405 nm).

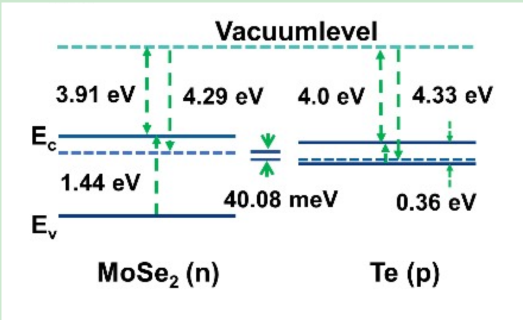

Fig. S10 Band alignment of p-Te/n-$MoSe_2$ heterostructure before contact.

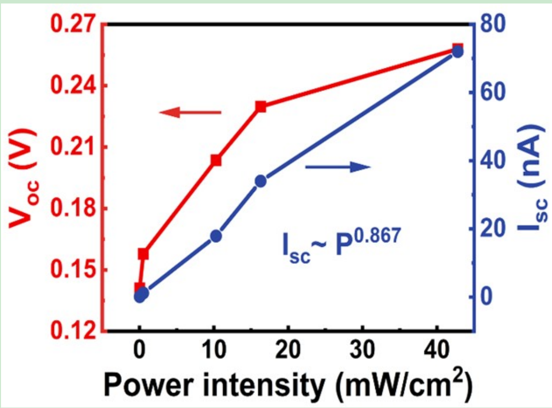

Fig. S11 Extracted I_{sc} and V_{oc} under different laser powers intensity of 405 nm.

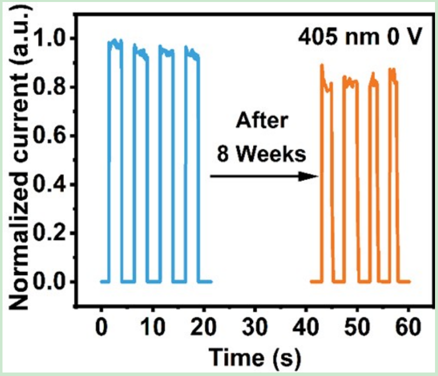

Fig. S12 Time-dependent photoresponse of the p-Te/n-$MoSe_2$ photodetector at zero bias voltage after 8 weeks storage.

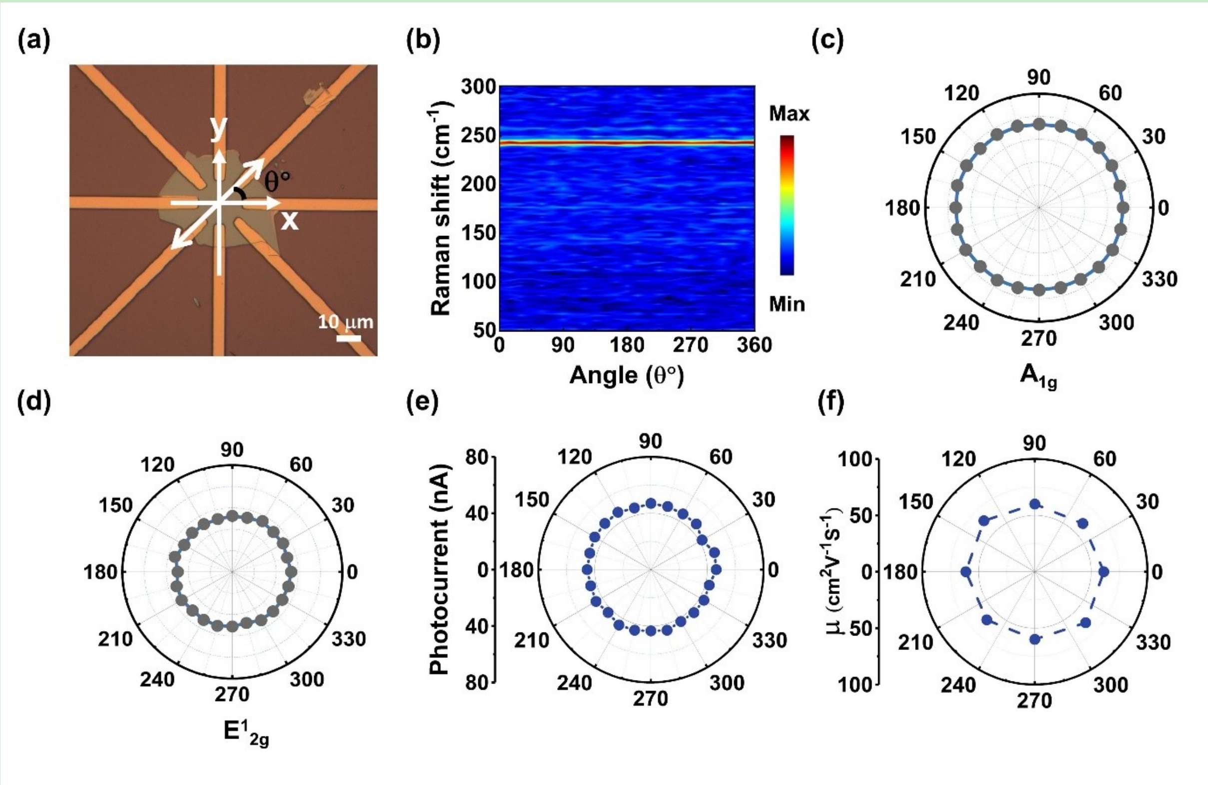

Fig. S13 (a) Optical image of the fabricated $MoSe_2$ FET device. (b) Polarized Raman intensity mapping of $MoSe_2$ nanosheet as a function of wave number and incident angle. (c) Polar plot of A_{1g} mode intensity in cross-polarized configurations. (d) Polar plot of E^1_{2g} mode intensity in cross-polarized configurations. (e) Polar diagram of the polarized photocurrent for the incident wavelengths of 405 nm (0.3 mW/cm^2) at 1 V. (f) Polar plots of the angle-dependent mobility as a function of the polarization angle.

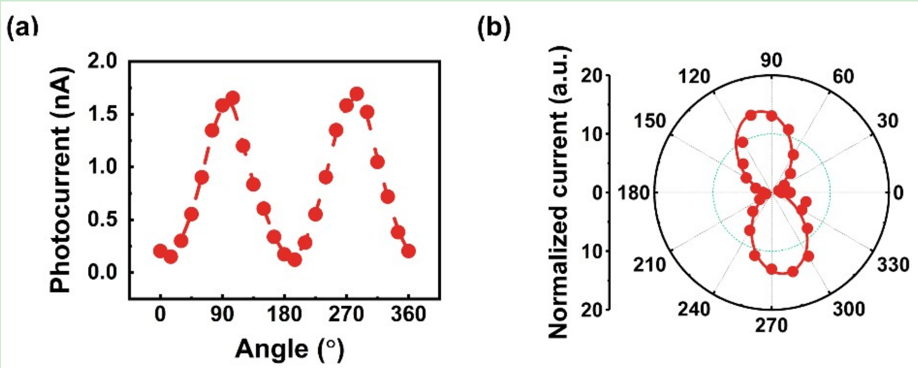

Fig. S14 Polarization-sensitive photodetection of p-Te/n-$MoSe_2$ heterostructure. (a) Polarized photocurrent under 0 V for the incident wavelengths 635 nm (5.968 mW/cm^2). (b) Polar diagram of the polarized photocurrent for the incident wavelengths of 635 nm at zero bias voltage, and the anisotropic ratio are 13.97.

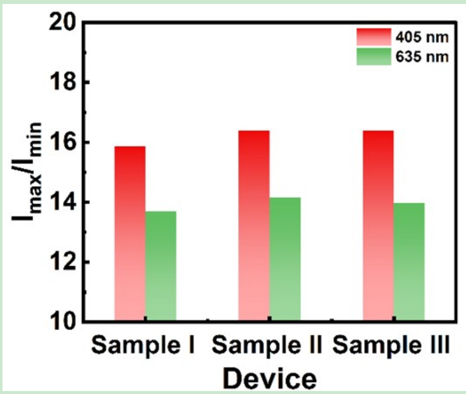

Fig. S15 The anisotropic ratio of another three constructed p-Te/n-$MoSe_2$ heterojunction device.

Table S1 Comparison of the device performances with previously reported 2D material-based photodetectors.

Material	Wavelength (nm)	voltage (V)	Responsivity (*R*) (mAW^{-1})	Detectivity (*D**) (Jones)	On/off ratio	Anisotropic ratio	Ref
Te/$MoSe_2$	405	0	2106	≈ 10^{13}	~10^5	15.87	This work
Te	1550	1	4.56 x 10^2	-	-	2.39	1
Te	400-1700	5	1.6 x 10^4	2.9 x 10^9	3 x 10^3	0.95	2
MoS_2	400-520	2	3500	2 x 10^{11}	-	2	3
Black phosphorus	1550	0.15	14.2	-	-	8.7	4
1T'-$MoTe_2$/T_d-$MoTe_2$	532-1060	0	0.4	1.07 x 10^8	-	2.72	5
GeSe/MoS_2	380-1064	0	105	1.46 x 10^{10}	3.6 x 10^4	2.95	6
MoS_2/GaAs	780	0	35.2	1.96 x 10^{13}		4.8	7

References

1 L. Tong, X. Huang, P. Wang, L. Ye, M. Peng, L. An, Q. Sun, Y. Zhang, G. Yang, Z. Li, F. Zhong, F. Wang, Y. Wang, M. Motlag, W. Wu, G. J. Cheng, W. Hu, Nat. Commun. 2020, **11**, 2308.

2 M. Amani, C. Tan, G. Zhang, C. Zhao, J. Bullock, X. Song, H. Kim, V. R. Shrestha, Y. Gao, K. B. Crozier, M. Scott, A. Javey, ACS Nano 2018, **12**, 7253.

3 L. Tong, X. Duan, L. Song, T. Liu, L. Ye, X. Huang, P. Wang, Y. Sun, X. He, L. Zhang, K. Xu, W. Hu, J. Xu, J. Zang, G. J. Cheng, Applied Materials Today 2019, **15**, 203.

4 P. K. Venuthurumilli, P. D. Ye, X. Xu, ACS Nano 2018, **12**, 4861.

5 J. Lai, X. Liu, J. Ma, Q. Wang, K. Zhang, X. Ren, Y. Liu, Q. Gu, X. Zhuo, W. Lu, Y. Wu, Y. Li, J. Feng, S. Zhou, J. Chen, D. Sun, Adv. Mater. 2018, **30**, 1707152.

6 Y. Xin, X. Wang, Z. Chen, D. Weller, Y. Wang, L. Shi, X. Ma, C. Ding, W. Li, S. Guo, R. Liu, ACS Appl. Mater. Inter. 2020, **12**, 15406.

7 C. Jia, D. Wu, E. Wu, J. Guo, Z. Zhao, Z. Shi, T. Xu, X. Huang, Y. Tian, X. Li, J. Mater. Chem. C. 2019, **7**, 3817.